




# Effects of Mn doping and sintering condition on the microstructure, dielectric, and energy storage properties of Ba<sub>0.8</sub>Sr<sub>0.2</sub>TiO<sub>3</sub> ceramics

Xinyuan Zhou<sup>1</sup>, Dan Xu<sup>1,\*</sup> , Taolin Yu<sup>1</sup>, Xiaoyang Duan<sup>1</sup>, Hong Zhao<sup>1</sup>, and Wenjie Zhao<sup>2,\*</sup>

<sup>1</sup>School of Science, Harbin University of Science and Technology, Harbin 150080, China

<sup>2</sup>Higher Educational Key Laboratory for Measuring & Control Technology, Instrumentations of Heilongjiang Province, Harbin University of Science and Technology, Harbin 150080, China

Received: 2 May 2023

Accepted: 29 June 2023

Published online:  
12 July 2023

© The Author(s), under exclusive licence to Springer Science+Business Media, LLC, part of Springer Nature 2023

## ABSTRACT

Mn<sup>2+</sup>ion, as an acceptor dopant, is usually employed to optimize the microstructures and electrical properties of BaTiO<sub>3</sub>-based lead-free ceramic systems. In this work, Ba<sub>0.8</sub>Sr<sub>0.2</sub>(Ti<sub>1-x</sub>Mn<sub>x</sub>)O<sub>3</sub> (BSTM,  $x = 0-0.005$  mol) ceramics were synthesized using the solid-state sintering technique. The effects of Mn<sup>2+</sup>doping content and sintering condition on the microstructure, dielectric, and energy storage properties of BSTM ceramics were studied and discussed. Compared with undoped samples, the Mn doping with a low concentration of  $x < 0.005$  mol can effectively reduce the average grain size of BSTM ceramics when sintered at 1300 °C/3 h. It is also found that Mn<sup>2+</sup> doping can decrease the dielectric loss and enhance remarkably the electrical strength ( $E_{BDS}$ ). This is because Mn replaces B-site Ti<sup>4+</sup> ions, thus generating oxygen vacancies as well as defect dipoles  $[Mn_{Ti}^{mn} - V_{\ddot{O}}]$ . With an increase in Mn<sup>2+</sup> doping content, more oxygen vacancies are produced to modify the microstructure and electrical properties. However, either elevated sintering temperature (e.g., 1325 °C) or prolonged sintering time (e.g., 1275 °C/5 h) can induce a rapid growth of grain size, leading to the weakened relaxation characteristics and the valence transformation from Mn<sup>2+</sup> to Mn<sup>3+</sup>/ Mn<sup>4+</sup>, but the energy efficiency of BSTM ceramics is enhanced due to the thin  $P$ - $E$  ferroelectric loops. The significant impacts of Mn<sup>2+</sup> doping and sintering conditions on the morphology structure and electrical properties need to be considered for the better optimization of energy storage properties of relaxor ferroelectric ceramics.

Address correspondence to E-mail: xudan@hrbust.edu.cn; zhaowenjie@hrbust.edu.cn

## 1 Introduction

Multilayer ceramic capacitors (MLCCs) are an important component in various electronic devices nowadays. Extensive investigations have been focused on the applications of dielectric properties, piezoelectric properties, and energy storage for MLCCs [1–4]. Among various lead-free perovskite materials for preparing MLCCs,  $(\text{Ba}_{1-x}\text{Sr}_x)\text{TiO}_3$  (BST) ceramics attract lots of attention owing to their excellent dielectric performance and tunable Curie temperature ( $T_C$ ) [5, 6]. Through controlling Sr content, the phase structure and dielectric and ferroelectric properties of BST ceramics can be modified to meet specific requirements of capacitor applications. Recently, as an acceptor dopant,  $\text{Mn}^{2+}$  is usually utilized for the optimization of the electrical properties of BT-based lead-free ceramics [7–11]. Many studies found that  $\text{Mn}^{2+}$  acceptor-doping caused oxygen vacancies  $V_{\text{O}}^{\bullet\bullet}$  in ceramics, resulting in forming  $[\text{Mn}^{2+}-V_{\text{O}}^{\bullet\bullet}]$  defect dipoles [7, 9, 10]. These results demonstrate that  $\text{Mn}^{2+}$  doping is conducive to improving leakage current, stabilizing dielectric constant, reducing dielectric loss, enhancing energy storage density, and lowering sintering temperature. For instance, Wang et al. reported that the leakage current was effectively suppressed in the 0.3 wt%  $\text{Mn}^{2+}$ -doped BT- $x$ BMH ceramics, and the  $x = 0.15$  sample exhibited excellent dielectric thermal stability [7]. Zhou et al. found that the  $[\text{Mn}^{2+}-V_{\text{O}}^{\bullet\bullet}]$  defect dipoles in the  $\text{Mn}^{2+}$ -doped 0.9BT-0.1BMN ceramics played a key role in improving breakdown electrical strength ( $E_{\text{BDS}}$ ) and energy efficiency ( $\eta$ ) [9]. Additionally, some researchers also found that  $\text{Mn}^{2+}$  ions could transform into  $\text{Mn}^{3+}$  and  $\text{Mn}^{4+}$  ions when the ceramics were sintered at elevated temperatures in the air [8, 11]. Chen et al. clarified the relations between the  $\text{Mn}^{2+}$  ion ratio in total Mn ions and  $\text{Ta}_2\text{O}_5$  dopant as well Mn ions occupation in the  $\text{ABO}_3$  lattice [8]. The solubility of  $\text{Mn}^{2+}$  ions in BT ceramics prepared by different routes had been well discussed [11]. However, the effects of  $\text{Mn}^{2+}$  doping and sintering condition on the structure, dielectric, and energy storage properties of BST ceramics have not yet been well investigated.

In the present work, the  $\text{Ba}_{0.8}\text{Sr}_{0.2}(\text{Ti}_{1-x}\text{Mn}_x)\text{O}_3$  (BSTM,  $x = 0-0.005$  mol) ceramics were designed and prepared. The effects of  $\text{Mn}^{2+}$  doping and sintering

condition on the microstructure and electrical properties of BSTM ceramics were analyzed based on the roles of multivalence Mn and  $[\text{Mn}^{2+}-V_{\text{O}}^{\bullet\bullet}]$  defect dipoles. Our results indicate that  $\text{Mn}^{2+}$  doping helps improve the dielectric loss, and enhance the  $E_{\text{BDS}}$  and energy density. High sintering temperature and prolonged sintering time facilitate grain growth, weaken the relaxation characteristics, and promote the valence transition of  $\text{Mn}^{2+}$ , but raise the energy efficiency of BSTM ceramics.

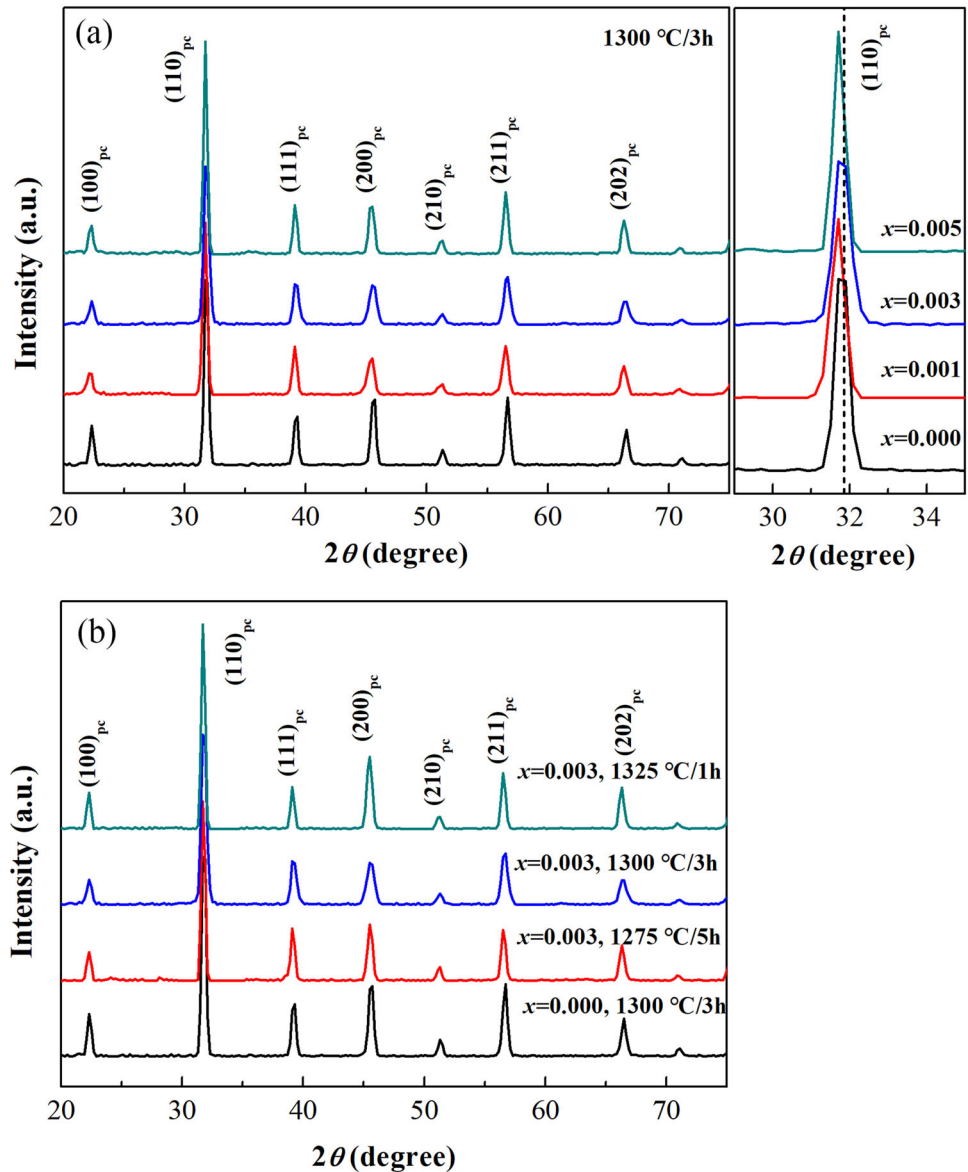
## 2 Experimental procedure

$\text{Ba}_{0.8}\text{Sr}_{0.2}(\text{Ti}_{1-x}\text{Mn}_x)\text{O}_3$  (abbreviated as BSTM $x$ ,  $x = 0.000, 0.001, 0.003, \text{ and } 0.005$  mol) ceramics were synthesized via a solid-state sintering technique. According to the chemical formula of BSTM $x$ , the raw material powders ( $\text{BaCO}_3$ ,  $\text{SrCO}_3$ ,  $\text{TiO}_2$ , and MnO with a purity > 99%, Aladdin, Shanghai) were weighed. First of all, the powders were thoroughly mixed in ethanol and ball-milled for 15 h. After that, the slurry was dried overnight, and the dried powders were calcined at 1100 °C for 3 h. Subsequently, the calcined powders were ball-milled once again for 15 h. The resultant powders were granulated thoroughly using a 5 wt% polyvinyl alcohol (PVA) binder and then pressed into pellets. The pellets with different compositions were finally sintered at 1300 °C for 3 h. Besides, in the case of  $x = 0.003$ , the pellet was also sintered at 1275 °C for 5 h and 1325 °C for 1 h for comparison. For dielectric breakdown measurement, the thickness of the BSTM samples is in the range of 0.17 ~ 0.20 mm. Test equipment and test conditions can be found in our previous work [12, 13].

## 3 Results and discussion

Figure 1a shows the XRD patterns of the  $\text{Ba}_{0.8}\text{Sr}_{0.2}(\text{Ti}_{1-x}\text{Mn}_x)\text{O}_3$  ceramics sintered at 1300 °C/3 h. In the  $2\theta$  range of 20°–75°, the main phases belong to perovskite pseudocubic (pc) phases, and impurities cannot be found in the BSTM $x$  ceramics. As the Mn content increases, the diffraction peaks (110) pc shift toward lower  $2\theta$  angles due to the larger  $\text{Mn}^{2+}$  ions (0.67Å) replacing the smaller  $\text{Ti}^{4+}$  ions (0.605Å) on the B-sites [8, 14], as revealed in the enlarged image on the right side of Fig. 1a.

**Fig. 1 a** XRD patterns of the  $\text{Ba}_{0.8}\text{Sr}_{0.2}(\text{Ti}_{1-x}\text{Mn}_x)\text{O}_3$  ceramics sintered at  $1300\text{ }^\circ\text{C}/3\text{ h}$  and **b** XRD patterns of the  $\text{Ba}_{0.8}\text{Sr}_{0.2}(\text{Ti}_{0.997}\text{Mn}_{0.003})\text{O}_3$  ceramics sintered at  $1275\text{ }^\circ\text{C}/5\text{ h}$ ,  $1300\text{ }^\circ\text{C}/3\text{ h}$ , and  $1325\text{ }^\circ\text{C}/1\text{ h}$

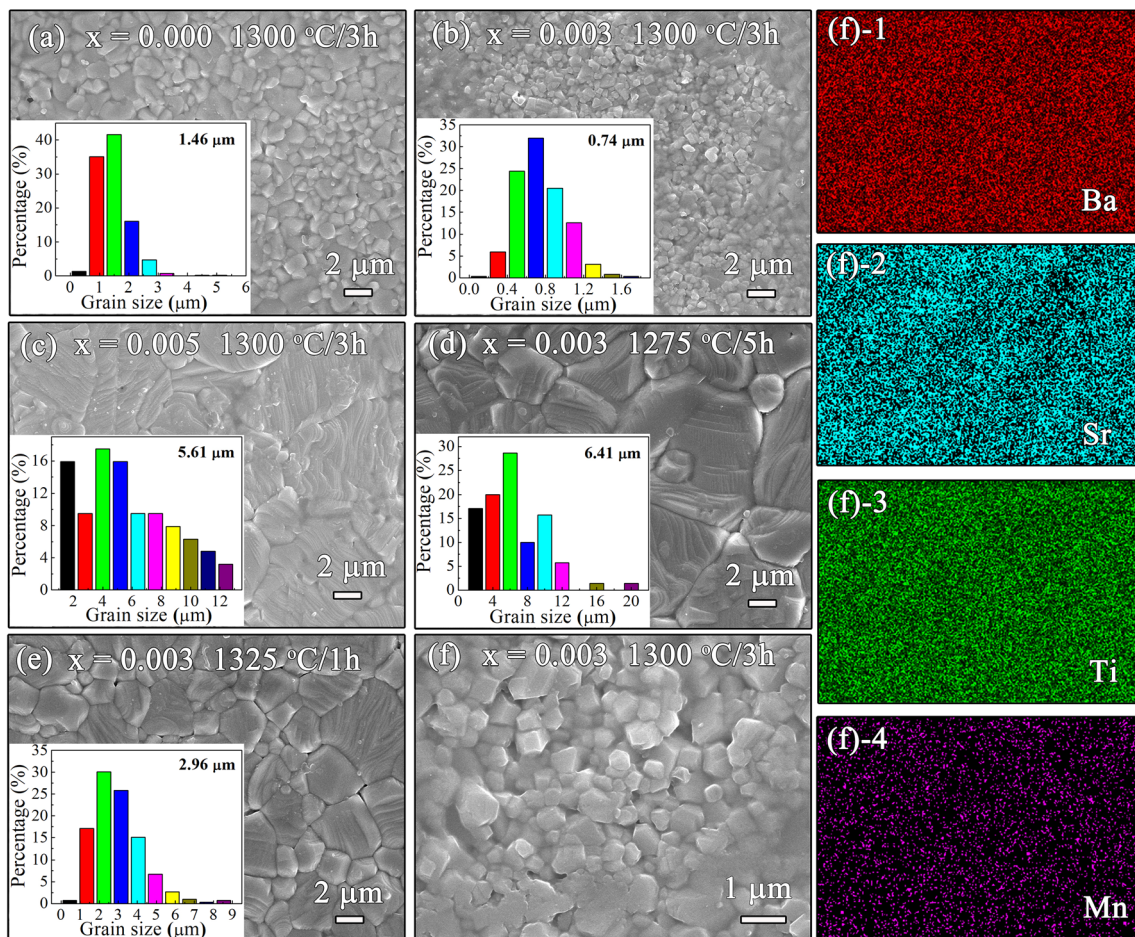


To optimize the sintering conditions, we prepared the  $\text{Ba}_{0.8}\text{Sr}_{0.2}(\text{Ti}_{0.997}\text{Mn}_{0.003})\text{O}_3$  ceramics sintered at  $1275\text{ }^\circ\text{C}/5\text{ h}$ ,  $1300\text{ }^\circ\text{C}/3\text{ h}$ , and  $1325\text{ }^\circ\text{C}/1\text{ h}$ , respectively. The corresponding XRD patterns of these ceramics are displayed in Fig. 1b. The pc-phase structure of  $\text{Ba}_{0.8}\text{Sr}_{0.2}(\text{Ti}_{0.997}\text{Mn}_{0.003})\text{O}_3$  ceramics is not altered, which is independent of the sintering conditions. The lattice parameters of BSTM ceramics obtained by Rietveld refinements are listed in Table 1. Under the same sintering condition of  $1300\text{ }^\circ\text{C}/3\text{ h}$ , the lattice parameters of BSTMx ceramics increase, and the volume expands as a whole with the Mn content. These refined results agree very well with the replacement of  $\text{Mn}^{2+}$  for  $\text{Ti}^{4+}$ .

Figure 2a–e shows SEM images of the surface of BSTM ceramics as a function of Mn content and sintering condition. The BSTM ceramics are dense and homogeneous at  $x \leq 0.003$  and the sintering condition of  $1300\text{ }^\circ\text{C}/3\text{ h}$ . However, as in the case of  $x > 0.003$  or a sintering condition of  $1275\text{ }^\circ\text{C}/5\text{ h}$  or  $1325\text{ }^\circ\text{C}/1\text{ h}$ , the grain size increases and grain distribution becomes uneven. The insets show the grain size distribution of BSTM ceramics. The average grain size of BSTM ceramics is  $1.46$ ,  $0.74$ , and  $5.61\text{ }\mu\text{m}$  for  $x = 0$ ,  $0.003$ , and  $0.005$  at  $1300\text{ }^\circ\text{C}/3\text{ h}$ ,  $6.41\text{ }\mu\text{m}$  for  $x = 0.003$  at  $1275\text{ }^\circ\text{C}/5\text{ h}$ , and  $2.96\text{ }\mu\text{m}$  for  $x = 0.003$  at  $1325\text{ }^\circ\text{C}/1\text{ h}$ , respectively. Compared to the undoped samples, a small amount of Mn doping helps to

**Table 1** Lattice parameters and fitting factors of BSTM ceramics

$x$ (mol)	Lattice parameters				R-factors		
	$a$ (Å)	$b$ (Å)	$c$ (Å)	$V$ (Å <sup>3</sup> )	$R_p$ (%)	$R_{wp}$ (%)	$R_{exp}$ (%)
0.000 @ 1300/3 h	3.9790 (3)	3.9790 (3)	3.9790 (3)	63.00	9.05	9.67	9.61
0.001 @ 1300/3 h	3.9901 (5)	3.9901 (5)	3.9901 (5)	63.53	11.03	11.16	10.01
0.003 @ 1300/3 h	3.9819 (5)	3.9819 (5)	3.9819 (5)	63.14	11.78	11.42	10.20
0.005 @ 1300/3 h	3.9887 (4)	3.9887 (4)	3.9887 (4)	63.46	10.76	11.25	10.32
0.003 @ 1275/5 h	3.9871 (3)	3.9871 (3)	3.9871 (3)	63.38	10.67	10.78	9.89
0.003 @ 1325/1 h	3.9867 (3)	3.9867 (3)	3.9867 (3)	63.36	9.33	9.06	10.91

**Fig. 2** SEM images of the surface of BSTM ceramics. Insets show the grain size distribution of BSTM ceramics. Figure 2f is the EDS mapping of BSTM ceramic with  $x = 0.003$  sintered at 1300 °C/3 h

reduce the grain size (Fig. 2b) [10], but when the doping content increases or the sintering temperature/ time increases, the grain size increases significantly. Among these affecting factors, the sintering time seems to dominate, e.g., the maximum average grain size of 6.41  $\mu\text{m}$  is obtained for  $x = 0.003$  at 1275 °C/5 h (Fig. 2d). High-temperature sintering is beneficial to the grain size growth; meanwhile, the longer

sintering time can promote the diffusion of oxygen vacancy in the BT lattice, and therefore, the large grains are observed in Fig. 2d and e [15]. The varied morphology is an indicator of the different electrical properties of BSTM ceramics [11]. Figure 2f shows the EDS mappings of  $\text{Ba}_{0.8}\text{Sr}_{0.2}(\text{Ti}_{0.997}\text{Mn}_{0.003})\text{O}_3$  ceramic sample sintered at 1300 °C/3 h. The Ba, Sr, Ti, and Mn elements distribute uniformly in the



Ba<sub>0.8</sub>Sr<sub>0.2</sub>(Ti<sub>0.997</sub>Mn<sub>0.003</sub>)O<sub>3</sub> ceramic, which indicates that Mn incorporates into the BSTM ceramics.

XPS curves of the O 1s for BSTM ceramics are shown in Fig. 3. For the ceramics sintered at 1300 °C/3 h (Fig. 3a and c), three fitting peaks are observed at around 530.8 eV, 532.0 eV, and 533.3 eV, respectively. The lowest binding energy originates from lattice oxygen (O<sub>L</sub>), and the middle fitting peak is assigned to oxygen vacancies (O<sub>V</sub>) [16, 17], while the higher fitting peak at 533.3 eV is associated with chemisorbed oxygen (O<sub>chem</sub>) on the ceramic samples' surface [18, 19]. Apart from the binding energies of O<sub>L</sub> and O<sub>V</sub>, however, the fitting peak at around 529.0 eV can also be observed in Fig. 3d and e, which is attributed to surface adsorbed oxygen-containing species (O<sub>A</sub>) [13]. Although O<sub>V</sub> does not directly represent the concentration of oxygen vacancies, the relative content of oxygen vacancies in different samples can be estimated using O<sub>V</sub>/O<sub>L</sub>, where O<sub>V</sub> and O<sub>L</sub> are the integrated areas of O<sub>V</sub> and O<sub>L</sub> fitting

curves, respectively. The calculated O<sub>V</sub>/O<sub>L</sub> ratio is 2.409, 8.171, and 6.936 for x = 0.001, x = 0.003, and x = 0.005 samples sintered at 1300 °C/3 h. The ratio is 2.978 at 1275 °C/5 h and 0.483 at 1325 °C/1 h for x = 0.003 samples. Overall, the O<sub>V</sub>/O<sub>L</sub> ratio displays an increasing trend with the increasing composition, but shows an obvious decreasing trend from 8.171 (x = 0.003 at 1300 °C/3 h) to 0.483 (x = 0.003 at 1325 °C/1 h) for different sintering condition, as shown in Fig. 3f.

The relations of O<sub>V</sub> content and acceptor Mn<sup>2+</sup> ions can be explained as follows. As Mn<sup>2+</sup> ions occupy the Ti<sup>4+</sup> site, oxygen vacancies will be generated to main charge neutrality, accompanied by the production of defect dipole [Mn<sup>2+</sup><sub>Ti</sub> - V<sup>••</sup>]. Earlier investigations demonstrate that a small amount of Mn<sup>2+</sup> doping helps reduce dielectric loss owing to the pinned effect of domain walls by defect dipole [Mn<sup>2+</sup><sub>Ti</sub> - V<sup>••</sup>] [8, 10, 11]. Additionally, the Mn<sup>2+</sup> doping can also remarkably restrain the valence transition from Ti<sup>4+</sup>

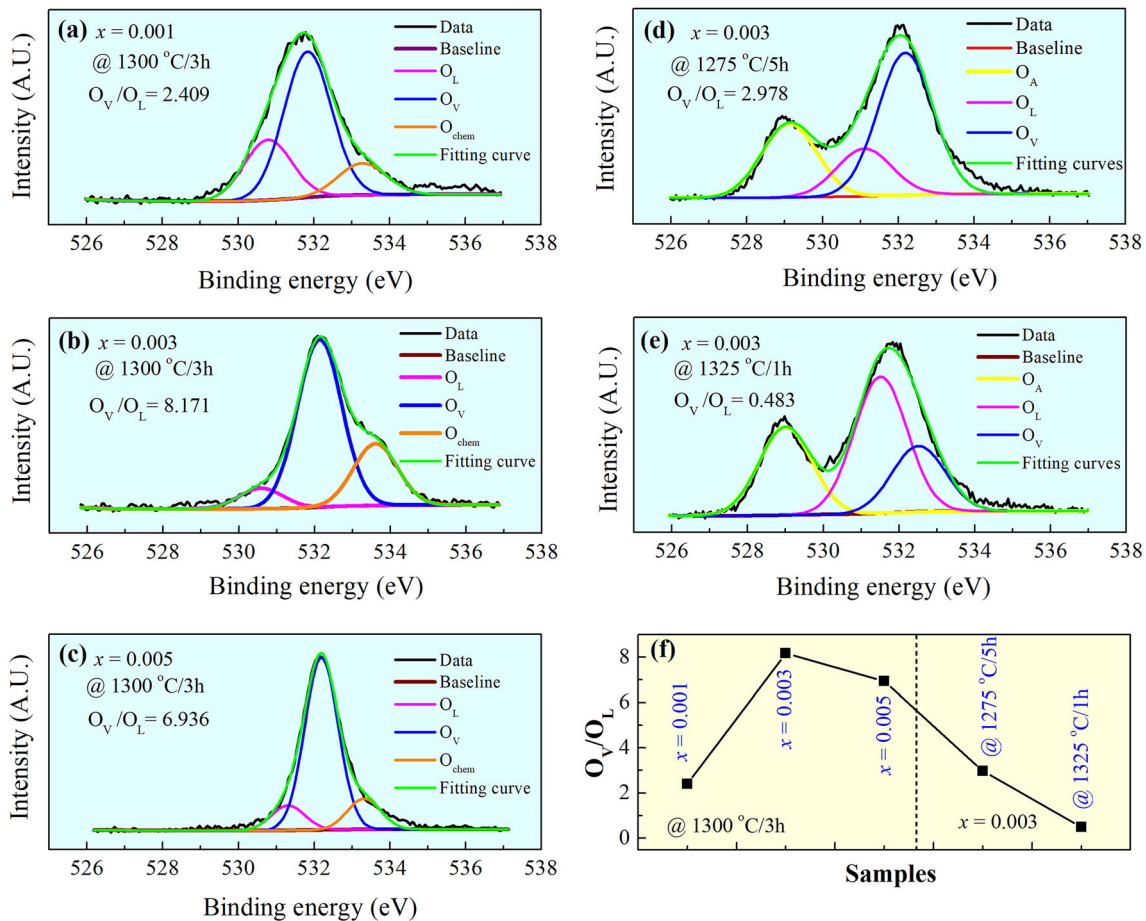


Fig. 3 XPS fitting results of O 1s narrow scan spectra for BSTM ceramics

to  $\text{Ti}^{3+}$ . If the valence of Mn is not changed during the sintering process, the oxygen vacancies would increase accordingly with the increasing  $\text{Mn}^{2+}$  doping content. Thus, a maximum  $O_V/O_L$  ratio of 8.171 is obtained for  $x = 0.003$  samples at 1300 °C/3 h. Thereafter, neither by increasing  $\text{Mn}^{2+}$  content nor by changing sintering conditions, the relative content of oxygen vacancies does not increase, but decreases significantly (Fig. 3f). This result indicates that some  $\text{Mn}^{2+}$  ions transform into  $\text{Mn}^{3+}$  and  $\text{Mn}^{4+}$  ions during the sintering process based on the following Eqs. (1) and (2).



The  $\text{Mn}^{3+}$  (0.53 Å) and  $\text{Mn}^{4+}$  (0.645 Å) ions can also substitute for B-site  $\text{Ti}^{4+}$  (0.605 Å) because of their similar ionic radii [8, 11]. We believe that the  $\text{Mn}^{2+}$  content is still predominant among the  $\text{Mn}^{2+}$ ,  $\text{Mn}^{3+}$ , and  $\text{Mn}^{4+}$  ions. Unfortunately, the most direct evidence is not obtained due to the very low Mn doping content in the ceramic samples.

Temperature dependences of dielectric constant ( $\epsilon_r$ ) and dielectric loss ( $\tan\delta$ ) of the  $\text{BSTM}_x$  ceramics sintered at 1300 °C/3 h are shown in Fig. 4a. The dielectric peak appears at around 60 °C and broadens with increasing Mn content. The increased local disorder at B-sites induced by Mn replacing Ti is responsible for the relaxation characteristics. Meanwhile, the Curie temperature  $T_c$  slightly decreases, accompanied by the remarkably reduced maximum dielectric constant  $\epsilon_m$ . In addition, the  $\tan\delta$  displays a very similar variation trend for all the samples with the content  $x$ . An abnormal loss peak can be observed in the vicinity of  $T_c$ , which is ascribed to the roles of some defect (e.g., oxygen vacancies,  $[\text{Mn}_{\text{Ti}}^{2+} - V_{\text{O}}]$ , etc.) migration at elevated temperatures [20, 21].

To illustrate the influences of sintering conditions on the dielectric temperature spectrum, Fig. 4b shows the temperature dependences of  $\text{Ba}_{0.8}\text{Sr}_{0.2}(\text{Ti}_{0.997}\text{Mn}_{0.003})\text{O}_3$  ceramics sintered at 1275 °C/5 h, 1300 °C/3 h, and 1325 °C/1 h measured at 1 MHz. The  $\text{Ba}_{0.8}\text{Sr}_{0.2}(\text{Ti}_{0.997}\text{Mn}_{0.003})\text{O}_3$  ceramics sintered at 1275 °C/5 h and 1325 °C/1 h exhibit a sharper Curie peak than the sample sintered at 1300 °C/3 h, and their  $\epsilon_m$  values are higher than the undoped sample. The sharp dielectric peak indicates that the two samples do not have dielectric relaxation characteristics, which can be confirmed by the large grain size shown

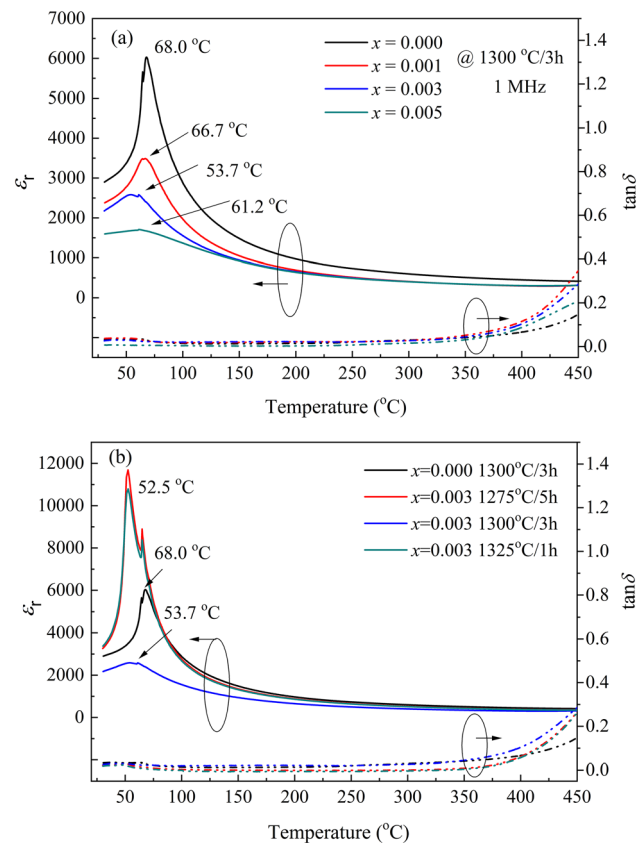


**Fig. 4** Temperature dependences of dielectric constant and dielectric loss for **a**  $\text{Ba}_{0.8}\text{Sr}_{0.2}(\text{Ti}_{1-x}\text{Mn}_x)\text{O}_3$  ceramics sintered at 1300 °C/3 h and **b**  $\text{Ba}_{0.8}\text{Sr}_{0.2}(\text{Ti}_{0.997}\text{Mn}_{0.003})\text{O}_3$  ceramics sintered at 1275 °C/5 h, 1300 °C/3 h, and 1325 °C/1 h measured at 1 MHz

in Fig. 2 and the ferroelectric loops in the following Fig. 7e and f. It is precise that the large grain size leads to a high dielectric constant. For the  $x = 0.003$  samples sintered at 1275 °C/5 h and 1325 °C/1 h, the second dielectric peaks are not intrinsic but are induced by the measurements, which will disappear during the cooling process (Fig. S1). In addition, it can also be observed that the  $\tan\delta$  values of  $\text{Ba}_{0.8}\text{Sr}_{0.2}(\text{Ti}_{0.997}\text{Mn}_{0.003})\text{O}_3$  ceramics sintered at 1275 °C/5 h and 1325 °C/1 h are lower than the others and maintain the thermal stability in a wide temperature range.

To better comprehend the relaxation characteristics of the BSTM ceramics, Fig. 5 shows temperature dependences of dielectric constant for the BSTM ceramics as a function of frequency. The frequency dispersion behavior can be observed in the  $x = 0.001$ ,  $x = 0.003$ , and  $x = 0.005$  samples sintered at 1300 °C/3 h. Moreover, an abnormal peak around 275 °C can

be observed in  $x = 0.005$  samples, which shifts toward to higher temperature with an increase in measuring frequency, demonstrating a thermal-activated relaxation behavior (Fig. 5d), which can be further confirmed by the cooling curves shown in Fig. S2. In addition, the modified Curie–Weiss equation is employed to estimate the diffusion coefficient ( $\gamma$ ) [22, 23]. The fitting curves of the modified Curie–Weiss equation at 10 MHz and the  $\gamma$  values are shown in Fig. 6. The  $\gamma$  values are 1.36, 1.55, and 1.37 for the  $x = 0.001$ ,  $x = 0.003$ , and  $x = 0.005$  samples sintered at 1300 °C/3 h, respectively. This reveals that Mn doping can enhance the relaxation characteristics of BSTM ceramics at 1300 °C/3 h when compared with the undoped samples. However, upon raising the sintering temperature (Fig. 6f) or extending the sintering time (Fig. 6e), the  $\gamma$  values decrease to 1.02 for the  $x = 0.003$  samples sintered at 1275 °C/5 h and 1325 °C/1 h, indicating that the two samples are normal ferroelectrics without relax or behavior. The high temperature and prolonged sintering time can weaken the relax or character and favor maintaining the normal ferroelectric state.

Figure 7 displays the  $P$ – $E$  loops of the BSTM ceramics with the increasing electric fields measured at room temperature. The undoped samples have a relatively low maximum testing field of 30 kV/cm. The Mn-doped samples, by contrast, possess a higher

breakdown strength ( $E_{BDS}$ ). This agrees well with the previous work. Furthermore, the more slim and square  $P$ – $E$  loops are acquired for the  $\text{Ba}_{0.8}\text{Sr}_{0.2}(\text{Ti}_{0.997}\text{Mn}_{0.003})\text{O}_3$  ceramics sintered at 1275 °C/5 h and 1325 °C/1 h measured at 10 Hz. A higher  $E_{BDS}$  is favorable for the recoverable energy density ( $W_{rec}$ ) of the BSTM ceramics, and thinner ferroelectric loops indicate a higher energy efficiency ( $\eta$ ) [7, 24], based on the following equations of energy storage (3–5).

$$W_{rec} = \int_p^{pm} E dp \tag{3}$$

$$W = \int_0^{Pm} E dp \tag{4}$$

$$\eta = 100\% \times \frac{W_{rec}}{w} \tag{5}$$

Apparently, larger  $P_m$ – $P_r$  and higher  $E_{BDS}$  values will contribute to larger  $W_{rec}$ . To investigate the impacts of  $\text{Mn}^{2+}$  content and defect dipoles on the  $P$ – $E$  loops of BSTM ceramics. The  $P_m$ ,  $P_r$ , and  $P_m$ – $P_r$  values of all the samples at the maximum electrical field are shown in Fig. 8. From Fig. 8, the  $P_r$  value firstly increases as  $x < 0.005$ , then decreases slightly for  $x = 0.005$ , and finally continuously increases for  $x = 0.003$  sintered at 1275 °C/5 h and 1325 °C/1 h. In the case of the sintering condition of 1300 °C/3 h, the maximum  $P_r$  is achieved at  $x = 0.003$ . This

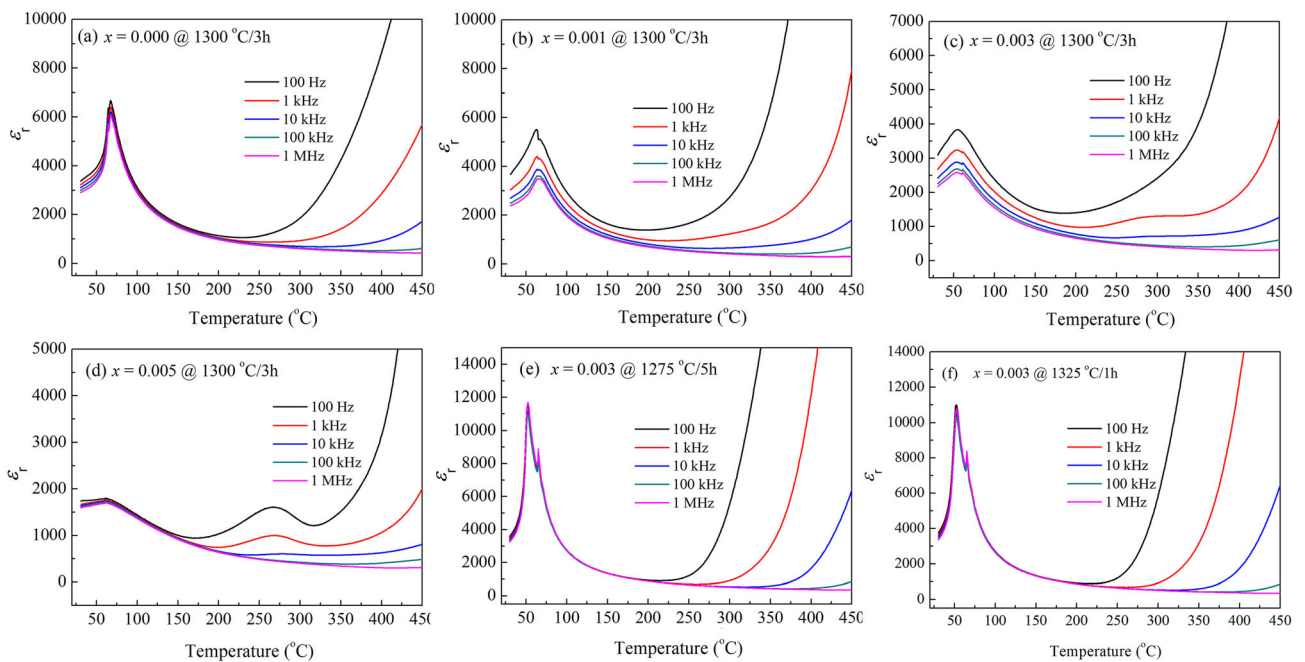
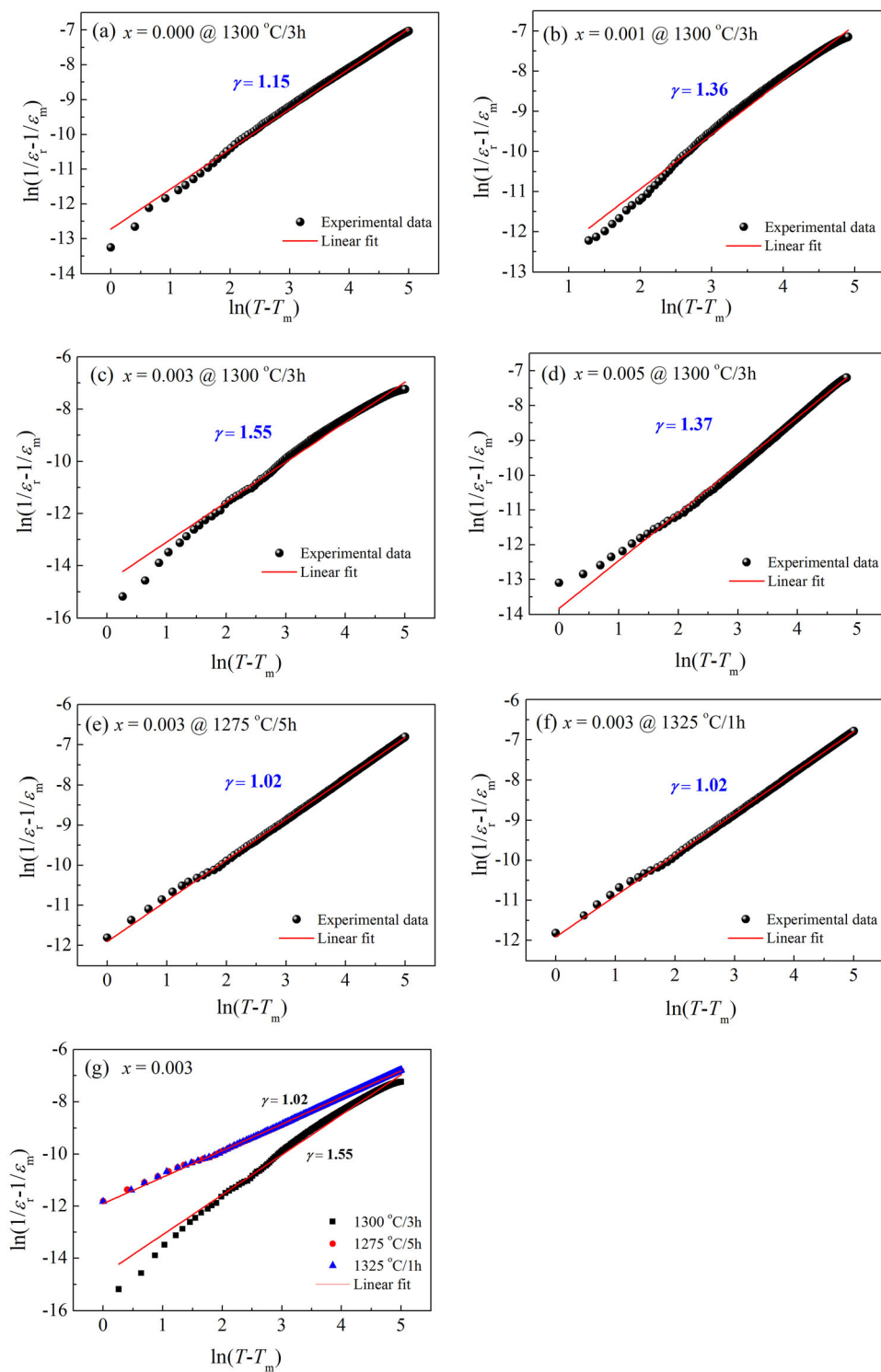


Fig. 5 Temperature dependences of dielectric constant for the BSTM ceramics as a function of frequency

**Fig. 6** The fitting curves of the modified Curie-Weiss equation at 10 MHz

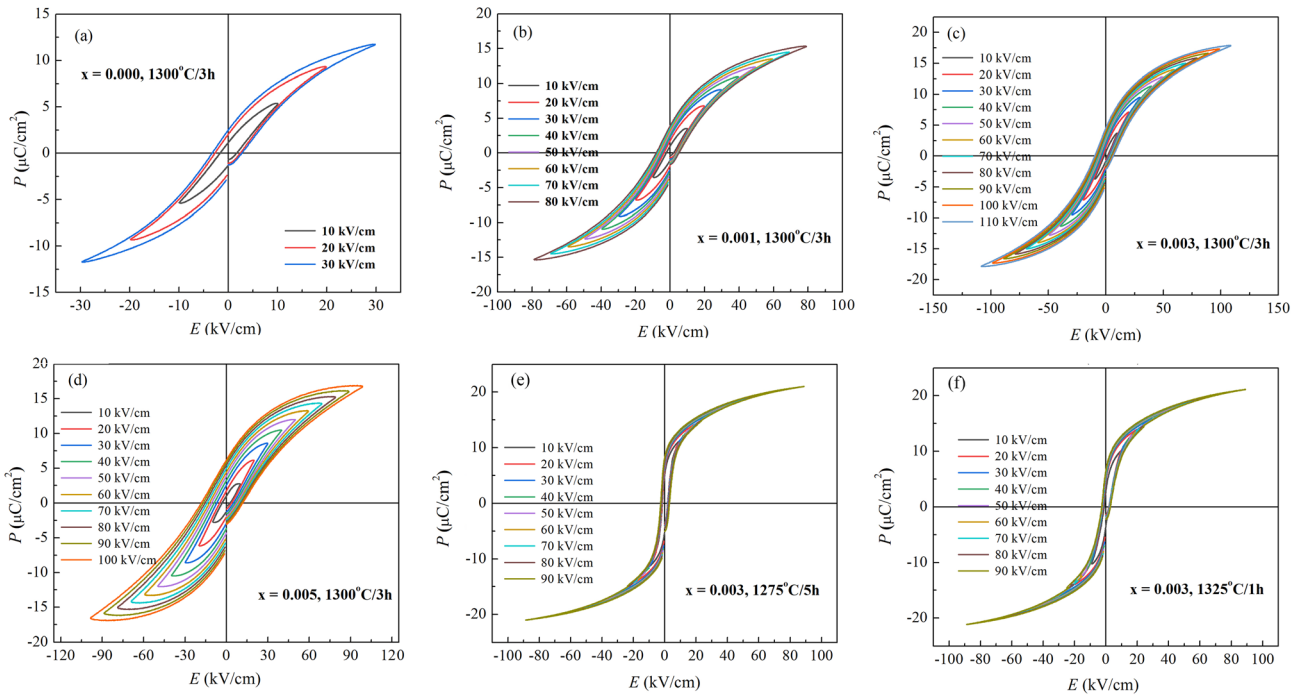


demonstrates that the defect dipoles can induce an improvement in polarization due to the contribution of defect dipole moment ( $P_D$ ), which is consistent with the XPS analysis. However, apart from the partial role of defect dipoles, the later increase in  $P_r$

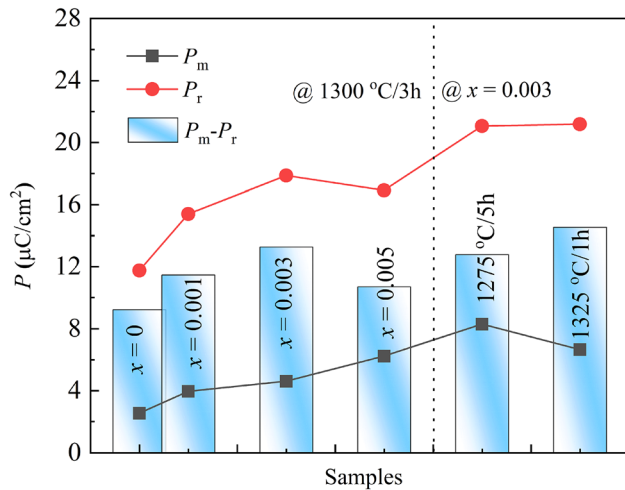
value can also be ascribed to the increased grain size for  $x = 0.003$  sintered at 1275 and 1325 °C/1 h.

Figure 9 shows the monopolar  $P$ - $E$  loops of the BSTM ceramics at the maximum electrical field. The  $W_{rec}$  values of the BSTM $x$  ceramics sintered at 1300





**Fig. 7** The  $P$ - $E$  loops of the BSTM ceramics with the different electric fields measured at room temperature



**Fig. 8** The  $P_m$ ,  $P_r$ , and  $P_m - P_r$  values of all the samples at the maximum electrical field

$^\circ\text{C}/3\text{ h}$  and  $\text{Ba}_{0.8}\text{Sr}_{0.2}(\text{Ti}_{0.997}\text{Mn}_{0.003})\text{O}_3$  ceramics sintered at  $1275^\circ\text{C}/5\text{ h}$  and  $1325^\circ\text{C}/1\text{ h}$  are 0.095, 0.268, 0.388, 0.286, 0.305, and 0.332  $\text{J}/\text{cm}^3$ , and the corresponding efficiency  $\eta$  is 60%, 53%, 54%, 35%, 71%, and 71%, respectively. Under the same sintering condition of  $1300^\circ\text{C}/3\text{ h}$ , the  $x = 0.003$  sample has the highest  $W_{\text{rec}}$  of 0.388  $\text{J}/\text{cm}^3$  with a lower  $\eta$  of 54% at 110  $\text{kV}/\text{cm}$ . Interestingly, the higher  $\eta$  of 71% is achieved for  $x = 0.003$  sample sintered at  $1275^\circ\text{C}/5\text{ h}$

and  $1325^\circ\text{C}/1\text{ h}$  without sacrificing energy density too much. Although further improvements are necessary for our energy storage results, the large impacts of sintering conditions on the morphology structure and electrical properties need to be considered for the better optimization of energy storage properties.

### 4 Conclusions

In summary,  $\text{Mn}^{2+}$ -doped  $\text{Ba}_{0.8}\text{Sr}_{0.2}\text{TiO}_3$  ceramics were prepared via a solid-state sintering technique. The influences of  $\text{Mn}^{2+}$  doping and sintering conditions on the microstructure, dielectric, and energy storage characteristics of  $\text{Ba}_{0.8}\text{Sr}_{0.2}\text{TiO}_3$  ceramics were investigated. All ceramic samples exhibit a pure perovskite structure with a pseudocubic (pc) phase without any impurities. A small amount of Mn doping favors the refinement of the grain size of BSTM ceramics. In addition,  $\text{Mn}^{2+}$  doping can also reduce the dielectric loss and enhance remarkably the electrical strength ( $E_{\text{BDS}}$ ). High sintering temperature and prolonged sintering time accelerate the grain growth, weaken the relaxation characteristics, and promote the valence transition of  $\text{Mn}^{2+}$ , but raise the energy efficiency ( $\eta$ ) of BSTM ceramics. Under the

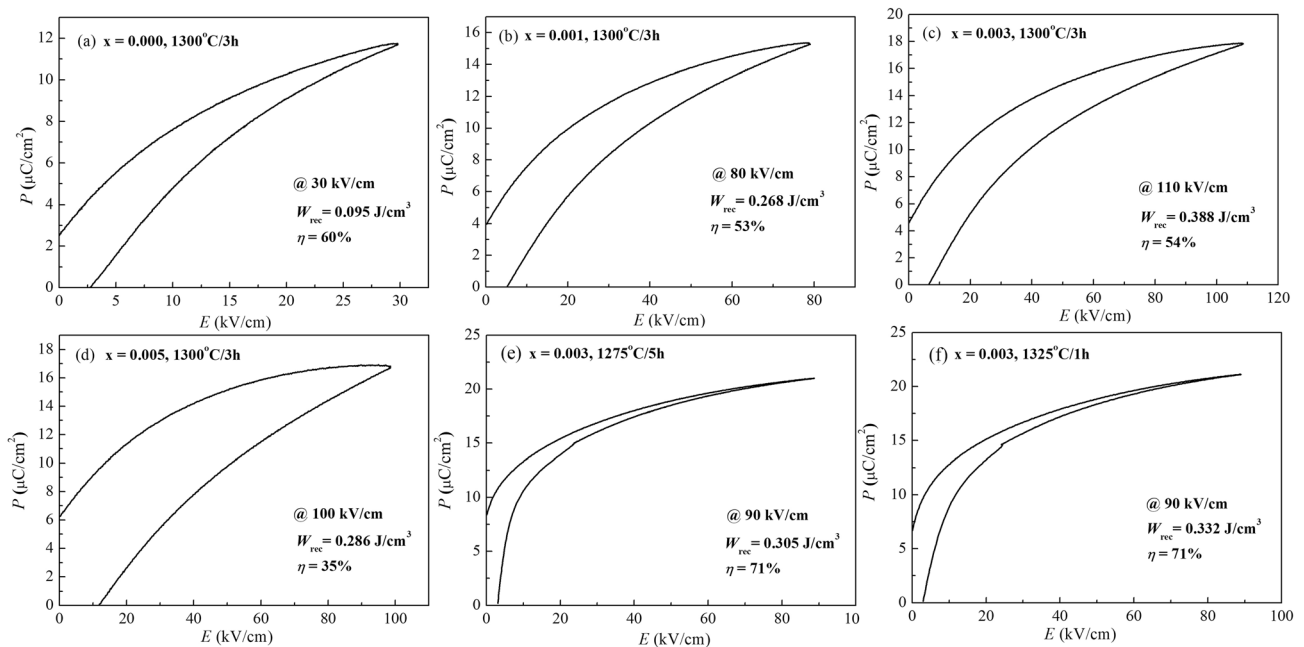


**Fig. 9** The monopolar  $P$ – $E$  loops of the BSTM ceramics at the maximum electrical field. Insets are the energy density  $W_{\text{rec}}$  and efficiency  $\eta$

same sintering condition of 1300 °C/3 h, the BSTM ceramic with the composition of  $x = 0.003$  obtains the highest  $W_{\text{rec}}$  of 0.388 J/cm<sup>3</sup> with a lower  $\eta$  of 54% at 110 kV/cm. By raising the sintering temperature or extending the sintering time, the energy efficiency of the  $x = 0.003$  samples can reach 71%. This result indicates that sintering conditions play a crucial role in modifying the morphology structure and electrical properties.

## Author contributions

DX and WZ contributed to the study conception and design. Material preparation, data collection, and analysis were performed by XZ, TY, and XD. The first draft of the manuscript was written by DX and HZ. All authors commented on previous versions of the manuscript, read, and approved the final manuscript.

## Funding

This work was financially supported by the National Natural Science Youth Foundation of China (Grant No. 51702069) and Natural Science Foundation of Heilongjiang Province (LH2019F026).

## Data availability

All data generated or analyzed during this study are included in this published article (and its supplementary information files).

## Declarations

**Competing interests** The authors have no relevant financial or non-financial interests to disclose.

**Supplementary Information:** The online version contains supplementary material available at <http://doi.org/10.1007/s10854-023-10918-5>.

## References

1. G. Luo, G. Zhang, Y. Zhang, A. Li, Y. Sun, R. Tu, Q. Shen, Wide temperature range of stable dielectric properties in relaxor BaTiO<sub>3</sub>-based ceramics by co-doping synergistic engineering. *Mater. Chem. Phys.* **302**, 127629 (2023)
2. W.P. Cao, W.L. Li, T.R.G.L. Bai, Y. Yu, T.D. Zhang, Y.F. Hou, Y. Feng, W.D. Fei, Enhanced electrical properties in lead-free NBT-BT ceramics by series ST substitution. *Ceram. Int.* **42**, 8438–8444 (2016)
3. S. Chang, C. Chen, X. Jiang, C. Zhao, J. Chen, Improved chemical defects, domain structure and electrical properties of BiFeO<sub>3</sub>–BaTiO<sub>3</sub> lead-free ceramics by simultaneous Na/Bi

- codoping and quenching process. *Ceram. Int.* **49**, 16191–16198 (2023)
4. S. Guan, H. Yang, S. Chen, Q. Chen, L. Yuan, X. Liu, L. Yang, G. Liu, G. Qiao, Effects of  $(\text{Bi}_{0.5}\text{Li}_{0.5})\text{TiO}_3$  addition on microstructures, electrical properties and thermal stability of  $\text{BiFeO}_3$ - $\text{BaTiO}_3$  piezoelectric ceramics. *Mater. Sci. Semiconduct. Process.* **156**, 107286 (2023)
  5. Q. Jin, Y.-P. Pu, C. Wang, Z.-Y. Gao, H.-Y. Zheng, Enhanced energy storage performance of  $\text{Ba}_{0.4}\text{Sr}_{0.6}\text{TiO}_3$  ceramics: influence of sintering atmosphere. *Ceram. Int.* **43**, S232–S238 (2017)
  6. Y.M. Li, J.J. Bian, Effects of reoxidation on the dielectric and energy storage properties of ce doped  $(\text{Ba}, \text{Sr})\text{TiO}_3$  ceramics prepared by hot-pressed sintering. *J. Eur. Ceram. Soc.* **40**, 5441–5449 (2020)
  7. C.Y. Wang, C. Liang, W.J. Cao, H.Y. Zhao, C.C. Wang, Boosting energy-storage efficiency and thermal stability via defect dipoles in  $\text{BaTiO}_3$ -based lead-free ceramics. *Ceram. Int.* **49**, 13330–13338 (2023)
  8. Z. Cen, Y. Zhen, W. Feng, P. Zhao, L. Chen, C. Zhu, X. Wang, L. Li, Improving piezoelectric properties and temperature stability for KNN-based ceramics sintered in a reducing atmosphere. *J. Am. Ceram. Soc.* **101**, 4108–4117 (2018)
  9. W.-B. Li, D. Zhou, L.-X. Pang, Enhanced energy storage density by inducing defect dipoles in lead free relaxor ferroelectric  $\text{BaTiO}_3$ -based ceramics. *Appl. Phys. Lett.* **110**, 132902 (2017)
  10. C. Zhu, Z. Cai, L. Li, X. Wang, High energy density, high efficiency and excellent temperature stability of lead free Mn-doped  $\text{BaTiO}_3$ - $\text{Bi}(\text{Mg}_{1/2}\text{Zr}_{1/2})\text{O}_3$  ceramics sintered in a reducing atmosphere. *J. Alloys Compd.* **816**, 152498 (2020)
  11. W. Chen, X. Zhao, J. Sun, L. Zhang, L. Zhong, Effect of the Mn doping concentration on the dielectric and ferroelectric properties of different-routes-fabricated  $\text{BaTiO}_3$ -based ceramics. *J. Alloys Compd.* **670**, 48–54 (2016)
  12. D. Xu, T.L. Yu, W.J. Zhao, W.P. Cao, W.L. Li, W.D. Fei, Enhancement in electrical and magnetic properties of  $(\text{Li}_{0.5}\text{Ga}_{0.5})^{2+}$  and  $(\text{Li}_{0.5}\text{Er}_{0.5})^{2+}$ -modified  $\text{BiFeO}_3$ - $\text{BaTiO}_3$  ceramics. *Ceram. Int.* **47**, 240202–224030 (2021)
  13. D. Xu, H. Zhao, T.L. Yu, X.Y. Duan, W.J. Zhao, Effects of Li/M (M = Al, Ga, In, and Er) co-doping on the electrical properties of  $\text{BiFeO}_3$ - $\text{BaTiO}_3$  ceramics. *J. Mater. Sci.* **33**, 22736–22750 (2022)
  14. R.D. Shannon, Revised effective ionic radii and systematic studies of interatomic distances in halides and chalcogenides. *Acta Cryst. A* **32**, 751–767 (1976)
  15. W.F. Liu, W. Chen, L. Yang, L.X. Zhang, Y. Wang, Ferroelectric aging effect in hybrid-doped  $\text{BaTiO}_3$  ceramics and the associated large recoverable electrostrain. *Appl. Phys. Lett.* **89**, 172908 (2006)
  16. Z. Hu, V. Koval, Y. Yue, M. Zhang, C. Jia, I. Abrahams, H. Yan, Structural evolution and coexistence of ferroelectricity and antiferromagnetism in Fe, Nb co-doped  $\text{BaTiO}_3$  ceramics. *J. Eur. Ceram. Soc.* **43**, 2460–2468 (2023)
  17. M.L. Wang, K. Xue, K. Zhang, L.X. Li, Dielectric properties of  $\text{BaTiO}_3$ -based ceramics are tuned by defect dipoles and oxygen vacancies under a reducing atmosphere. *Ceram. Int.* **48**, 22212–22220 (2022)
  18. L. Yang, C. Chen, X. Jiang, X. Huang, X. Nie, S. Chang, Enhanced ferroelectric and piezoelectric properties of  $\text{BiFeO}_3$ - $\text{BaTiO}_3$  lead-free ceramics by simultaneous optimization of Bi compensation and sintering conditions. *Ceram. Int.* **48**, 12866–12874 (2022)
  19. C. Yu, Y. Zeng, B. Yang, R. Wylde, R. Donnan, J. Wu, J. Xu, F. Gao, I. Abrahams, M. Reece, H. Yan,  $\text{SrFe}_{12}\text{O}_{19}$  based ceramics with ultra-low dielectric loss in the millimetre-wave band. *Appl. Phys. Lett.* **112**, 143501 (2018)
  20. L.J. Liu, M.X. Wu, Y.M. Huang, Z. Yang, L. Fang, C.Z. Hu, Frequency and temperature dependent dielectric and conductivity behavior of  $0.95(\text{K}_{0.5}\text{Na}_{0.5})\text{NbO}_3$ - $0.05\text{BaTiO}_3$  ceramic. *Mater. Chem. Phys.* **126**, 769–772 (2011)
  21. S.Y. Zheng, D.P. Shi, L.J. Liu, G.Z. Li, Q.C. Wang, L. Fang, B. Elouadi, Oxygen vacancy-related dielectric relaxation and electrical conductivity in La-doped  $\text{ba}(\text{Zr}_{0.9}\text{Ti}_{0.1})\text{O}_3$  ceramics. *J. Mater. Sci.* **25**, 4058–4065 (2014)
  22. M. Zhou, R. Liang, Z. Zhou, X. Dong, A novel  $\text{BaTiO}_3$ -based lead-free ceramic capacitors featuring high energy storage density, high power density, and excellent stability. *J. Mater. Chem. C* **31**, 8528–8537 (2018)
  23. W.J. Qin, M. Zhao, Z.M. Li, D.Y. Zhang, M.L. Zhang, Y.H. Xu, L. Jin, Y.X. Yan, High energy storage and thermal stability under low electric field in  $\text{Bi}_{0.5}\text{Na}_{0.5}\text{TiO}_3$ -modified  $\text{BaTiO}_3$ - $\text{Bi}(\text{Zn}_{0.25}\text{Ta}_{0.5})\text{O}_3$  ceramics. *Chem. Eng. J.* **443**, 136505 (2022)
  24. S.J. Liu, Q.D. Xie, L.X. Zhang, Y.Y. Zhao, X. Wang, P. Mao, J.P. Wang, X.J. Lou, Tunable electrocaloric and energy storage behavior in the ce, Mn hybrid doped  $\text{BaTiO}_3$  ceramics. *J. Eur. Ceram. Soc.* **38**, 4664–4669 (2018)
- Publisher's Note** Springer Nature remains neutral with regard to jurisdictional claims in published maps and institutional affiliations.
- Springer Nature or its licensor (e.g. a society or other partner) holds exclusive rights to this article under a publishing agreement with the author(s) or other rightsholder(s); author self-archiving of the accepted manuscript version of this article is solely governed by the terms of such publishing agreement and applicable law.